Research paper

Impact of aluminum on the Seebeck coefficient and magnetic properties of La$_{0.7}$Ba$_{0.3}$MnO$_3$ manganites

H.F. Mohamed[a,b,*], A.M. Ahmed[a,*], A.K. Diab[a], Esraa Y. Omar[a]

[a] Physics Department, Faculty of Science, Sohag University, 82524 Sohag, Egypt
[b] Key Laboratory of Materials for High Power Laser, Shanghai Institute of Optics and Fine Mechanics, Chinese Academy of Sciences, Shanghai 201800, China

HIGHLIGHTS

- Al effect on the thermopower and magnetic susceptibility of La$_{0.7}$Ba$_{0.3}$MnO$_3$ compound.
- The composites are still a single phase rhombohedral despite adding Al$_2$O$_3$ phase.
- Power factor values decrease with increasing Al content.
- (LaBaMnO)$_{0.975}$/(AlO)$_{0.025}$ composite record the highest value of power factor.
- TEP data satisfy the Magnon and Phonon drag model and SPH conduction mechanism.

ABSTRACT

The effect of aluminum on $(La_{0.7}Ba_{0.3}MnO_3)_{1-x}/(Al_2O_3)_x$ composites is investigated based on their crystal structure, thermoelectric power and magnetic properties. The X-ray diffraction process reveals that the composite still exhibits a rhombohedral perovskite structure (R$\bar{3}$C) of all composites. The thermoelectric power data satisfies the Magnon and Phonon-drag models in the low-temperature range, and the smaller Polaron conduction mechanism in the high-temperature range. The power factor values decrease with Al content and the x = 0.025 record the highest value. All composites undergo ferromagnetic to paramagnetic transition at a certain temperature T$_C$. The AC susceptibility values decrease with the increasing Al content.

1. Introduction

Thermoelectric power (TEP) materials are used to produce electricity from waste heat. The ability of these materials to convert heat into electricity is evaluated by their figure of merit $ZT = \sigma S^2 T/\lambda$, where S, σ, T, and λ, are the Seebeck coefficient, electrical conductivity, temperature, and thermal conductivity, respectively [1,2]. In some previous studies, several compounds have been reported with high ZT values [3–5].

Regardless of their high ZT values, these compounds have partial practical use because of their low chemical stability in air at high temperatures. The thermal technologies used in industries depend on development of thermal bulk materials, which have electric thermal low cost, thermal stability at high temperatures in air, and are environmentally friendly. Recently, thermoelectric bulk manganites have gained significant attention because they realize the above-mentioned requirements. Since the discovery of a colossal value of Seebeck

coefficient for Gd−Sr manganites [6], extensive research has been conducted on manganites. For example, the n-type Ca−Sr−Yb−Mn−O [7] manganites were studied and it was observed that they have electrons as dominant carriers for all temperature ranges. Furthermore, this compound exhibited a very high power factor value that reaches up to $0.22\,\mathrm{mW\,m^{-1}\,K^{-2}}$ at 773 K. Therefore, n-type manganites with good conductivity and Seebeck coefficient are required for power generation in industries. Despite exhibiting intriguing electric and magnetic properties [8], Barium manganese perovskites have not gained much attention. In $Pr_{2/3}(Ba_{1-x}Cs_x)_{1/3}MnO_3$ manganites, the thermoelectric properties are deteriorated by cesium dopant because of the decreasing charge carriers [9]. The LaBaMnO/AlO compound investigated in this study exhibits properties similar to those of other thermoelectric manganites. By choosing the right dopant, the different factors of ZT can be tuned to improve its value. Aluminum (Al) is considered to be a promising dopant because it causes disorder among the Mn ions, reduces κ, and favors metallicity. The magnetic susceptibility $\chi\,(T)$ of the

Fig. 1. (a) XRD patterns of LBMO/Al$_2$O$_3$, where $0.0 \leq x \leq 0.15$ wt% at room temperature. Inset figure of (a) show enlarged view of the (2 0 2) and (0 0 6) peaks. Figures of (b) and (c) show the Rietveld refined pattern and the inset show the crystal shape of the composite of x = 0 with 0.15 wt%, respectively.

Table 1
Rietveld refined of (La0.70Ba0.3MnO3)1-x/(Al2O3)x, where x = 0, 0.025, 0.050, 0.075, 0.10, 0.125 and 0.150 wt%) manganite system (with space group) at room temperature.

(La$_{0.70}$Ba$_{0.3}$MnO$_3$)$_{1-x}$/(Al$_2$O$_3$)$_x$	0	0.025	0.050	0.075	0.10	0.125	0.150
Cell parameter							
a(Å) = b(Å)	5.5369	5.5329	5.53701	5.55475	5.54027	5.5278	5.54083
c(Å)	13.5539	13.5324	13.5379	13.5578	13.5456	13.5397	13.53169
Volume (Å3)	359.861	358.778	359.446	362.28	360.074	358.309	359.776
Bond length							
La/(Ba−O)	2.540	2.578	2.626	2.626	2.583	2.564	2.534
Mn−O (Å)	1.970	1.965	1.960	1.960	1.965	1.968	1.970
The electronic bandwidth (W)	0.0931	0.0939	0.0947	0.0947	0.0934	0.0939	0.0935
Average crystal size							
average crystallite size ‹CS› nm	25.82	29.62	31.09	29.56	25.78	31.41	27.36
Average grain size ‹GS› nm	648.415		330.88		158.73		463.23
R-factor (%)							
R$_f$	5.55	6.26	7.25	6.85	6.66	6.94	7.02
R$_{Bragg}$	5.35	5.39	6.62	6.66	5.24	5.77	5.23
Goodness of fit indicator χ	1.31	1.23	2.64	1.72	1.04	1.84	2.09

hole doping level in the LaMnO sample provides an important information about its valence and the concentration of magnetic ions and their variations during the transition phase. It was observed that the Curie temperature (T_C) is independent of the grain size [10]. Several studies [11–14] reported the transition from the ferromagnetic (FM) ordering to the spin-glass state or superparamagnetism according to the change in LMO microstructure from coarse-grained to nanocrystalline. The magnetic properties and TEP of the LaBaMnO/AlO compounds have not been studied previously. Therefore, we considered

investigating the effect of Al$_2$O$_3$ doping on the TEP and magnetic susceptibility for LBMO.

2. Experimental

The present study, (La$_{0.7}$Ba$_{0.3}$MnO$_3$)$_{1-x}$/(Al$_2$O$_3$)$_x$ composites with × = 0–0.15 wt% step 0.025 were prepared in two stages. In the first stage, the La$_{0.7}$Ba$_{0.3}$MnO$_3$ powders were prepared in a desired ratio of the conventional solid-solid reaction method. The first chemicals,
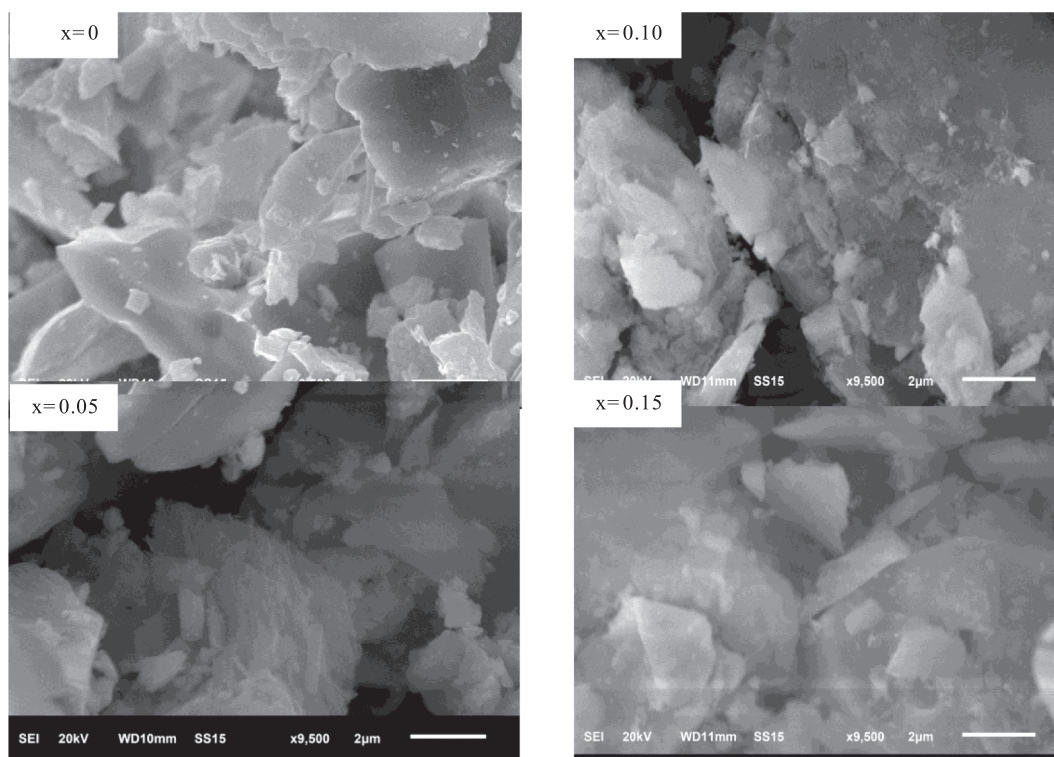
Fig. 2. SEM micrographs of LBMO/Al$_2$O$_3$ composites, where x = 0, 0.05, 0.10, and 0.15.

i.e., La$_2$CO$_3$, BaO, and MnCO$_3$ (high purity powder; 99.99%) were mixed in stoichiometric amount to prepare the mother compound (La$_{0.7}$Ba$_{0.3}$MnO$_3$). The mixture was milled for 6 h to ensure homogeneity and was pressed into pellets under a pressure of 5 ton cm^{-2}. The tablets were calcined for 24 h at 1173 K, and then milled in the identical conditions. The tablets were milled; combined; and subsequently, sintered in air at 1473 K for 48 h. The resultant LBMO powders had a single-phase perovskite structure. In the second stage, suitable quantities of the resultant La$_{0.7}$Ba$_{0.3}$MnO$_3$ (LBMO and Al$_2$O$_3$ (high purity; 99.9 9%) powders were completely combined and milled. Lastly, the combination was palletized at a pressure of 5 tons cm^{-2} and then repeated sintered at 1173 K for 4 h. The structural characterization was performed through X-ray diffraction (*XRD*) with Cu Kα radiation at room temperature. The microstructures of the composites were considered by JEOL JSM-6610LV scanning electron microscope (SEM). The TEP measurements were examined using a home-built set up published in our previous researches [15–17]. The AC susceptibility of the composites was measured over the 100–400 K temperature range under a magnetic field of 250 µT and frequency of 0.3 kHz using the Barrington Instruments MS2/MS3 susceptibility system.

3. Results and discussion

3.1. Structural properties

XRD examination is a highly significant technique used for phase identification and analysis. Fig. 1(a) shows the XRD patterns for (La$_{0.7}$Ba$_{0.3}$MnO$_3$)$_{1-x}$/(Al$_2$O$_3$)$_x$ composites, where 0 ≤ x ≤ 0.15 wt%. %. It is observed that all composites have a single-phase rhombohedral structure with a space group(R$\bar{3}$C), and no second (Al$_2$O$_3$) or impurity phase detectable. All reflection peaks of the (La$_{0.7}$Ba$_{0.3}$MnO$_3$)$_{1-x}$/ (Al$_2$O$_3$)$_x$ composite satisfies the LaBaMnO phase and remains unshifted, owing to no reaction occurs between the Al$_2$O$_3$ material and LBMO matrix. Otherwise, a slight shift to the lower angle for x = 0.075 wt% means that this composite has the largest cell volume

(the inset of Fig. 1-a). It can be interpreted that some part of Al$_2$O$_3$ goes into the perovskite lattice replacing Mn in the LBMO matrix. The large ionic radius of Al^{3+} (0.675 Å) with Mn^{3+} (0.53 Å) causes the lattice parameter to expand (Table 1). The inset of Fig. 1(a) displays an enlarged view of the (2 0 2) and (0 0 6) peaks near 39°. It is evident that the double-split peak gradually changes as the Al content increases, thereby indicating a structural phase transition to low symmetry. The X-ray data analyzed with the Fullproof software calculate the cell parameters, which are tabulated in Table 1. Typical plots of the XRD pattern (Fig. 1, -b, -c), with its Rietveld refined pattern, confirm a rhombohedral lattice with a space group (R$\bar{3}$C), in which the La/Ba atoms are located at 6a (0, 0, 0.25), Mn/Al at 6b (0, 0, 0), and O at 18e (x, 0, 0.25) Wyckoff positions. Besides, it includes the difference between the observed and calculated patterns as well as the crystal shape of the composite. The approximate values of average crystallite size ⟨*CS*⟩ is estimated using the Debye Scherer formula,

$$\langle CS \rangle = \frac{0.89\lambda}{\beta cos(\theta)} \tag{1}$$

where λ is the wavelength of the X-ray, β is a full width at half-maximum (FWHM) of the XRD peak in radians (β = $\sqrt{\beta_o^2 - \beta_{LaB6}^2}$, where β$_o$ is measured for the composites and β$_{LaB6}$ corresponds to the standard (LaB$_6$) sample) [18], and θ is the Bragg angle. The size and grain morphology was determined by the SEM images of the (La$_{0.7}$Ba$_{0.3}$MnO3)$_{1-x}$/(Al$_2$O$_3$)$_x$ composites, as shown in Fig. 2. The grains exhibit a coarse structure. Overall, the crystallite size (determined from XRD) is in the range of 25.8–31.9 nm, as the grain sizes (determined from SEM) are much larger, 358.3–362.3 nm (Table 1). This difference is probably because of the fact that an LBMO grain consists of several crystallites and/or the internal-stress and defects in the structure [19]. Numerous crystal/grain sizes for both XRD and SEM have their sequence disturbed with change in the Al content. Moreover, the lattice parameters and the unit-cell volume altered slowly with the increasing Al$_2$O$_3$ content (as seen in Table 1), where the rate of change for a = (5.53–5.54 Å) and for V = (357–359 Å^3). This clarifies that the lattice is
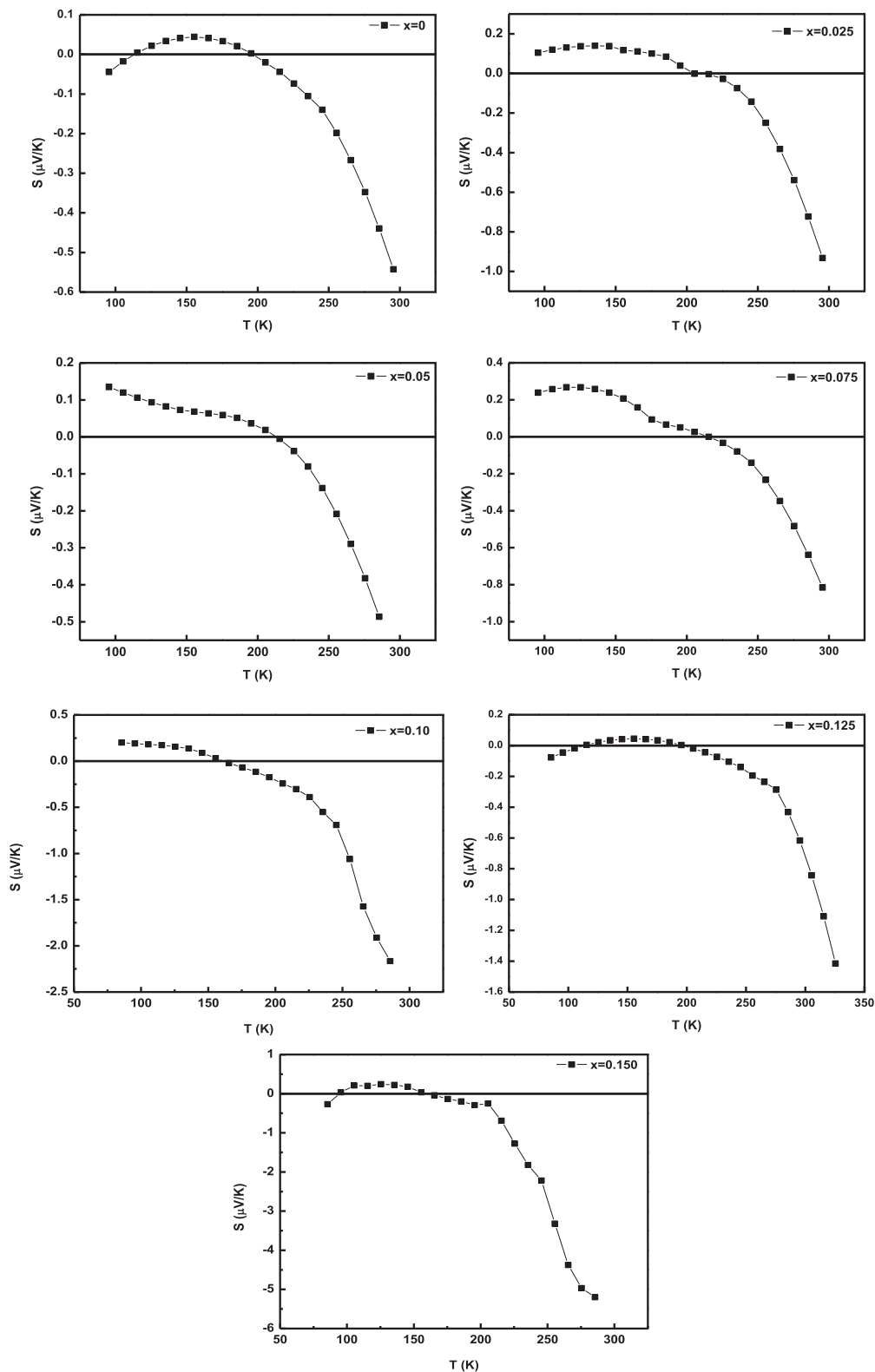
Fig. 3. Seebeck coefficient versus T for the prepared samples of LBMO/Al$_2$O$_3$ composites, where $0 \le x \le 0.15$.

almost unchanged. This is because the ionic radius of the Al^{3+} ion is larger than that of Mn^{3+}. Therefore, it finds it difficult to enter into the lattice and is pushed out toward the grain boundary to release the local strain. This is also confirmed by a slight change in the Mn−O bond length (determined from the Rietveld refinement presented in Table 1).

3.2. Thermopower properties

The Seebeck coefficient of the $(La_{0.7}Ba_{0.3}MnO_3)_{1-x}/(Al_2O_3)_x$ composites, as a function of temperature, is shown in Fig. 3. All composites showed both the signs of S, one is a positive in lower temperatures and the other is negative in higher temperatures. The S value is in the

Table 2
The thermal activation (Es) energy, electrical activation (Eρ) energy, the (B) parameter and the small polaron hopping energy (WH) for $(La_{0.70}Ba_{0.3}MnO_3)_{1-x}/(Al_2O_3)_x$ composites.

$(La_{0.70}Ba_{0.3}MnO_3)_{1-x}/(Al_2O_3)_x$	WH (meV)	Eρ (meV)	B	Es (meV)
0	78.66	107.18	−0.1018	28.51
0.025	16.13	28.78	−0.0520	12.65
0.050	51.87	60.07	−0.0336	8.19
0.075	41.53	53.79	−0.0495	12.26
0.10	101.73	107.90	−0.1031	6.17
0.125	104.84	114.59	−0.1994	9.74
0.150	128.78	139.72	−0.0478	10.93

microvolt range and exhibits a crossover from positive to negative sign at a certain temperature (transition temperature (T_s)). This means that the conduction is governed by the mixed charge carriers of electrons and holes.

This crossover from hole to electron conduction is because of the excitation of electrons from the valence band (VB) t_{2g} to the conduction band (CB) e_g. The high electron mobility in the CB leads to negative S; whereas, the e_g band is in full spin polarized FM non-degenerated state and S shows a positive value [20]. At low temperatures, the electrons in the VB band are excited into the impurity band, which generates hole like carriers, which is accountable for the positive S.

The TEP data of the present samples in the semiconductor regime are fitted to the Mott's Polaron hopping equation [21].

$$S = \pm k_B/e(\Delta E_s/k_B T + B) \tag{2}$$

where k_B is the Boltzmann constant, e is the electronic charge, E_S is the activation energy obtained from the data, and B is a constant. In Eq. (2), B < 1 implies the applicability of the small Polaron hopping (SPH) model, whereas B > 2 indicates large Polaron hopping. From the slope and the intercept of S versus 1/T curves, E_s and B were calculated and tabulated in Table 2. The value of E_s decreases for x ≤ 0.05 and changes randomly for x ≥ 0.075. The activation energy E_s is observed to be maximum in case of the parent compound. The Polaron hopping energy (W_H) value of the composites has been determined in terms of difference in the activation energies with $W_H = E_\rho - E_s$ (where $E_s < E_\rho$).

E_ρ is the sum of the activation energy required for creating the carriers and activating their hopping process (determined from the ρ-T curves), and E_s is the energy required to activate only those carriers that are hopping. The large difference between the activation energies E_ρ and E_s is the distinctive feature of the SPH conduction. Besides, the obtained value of B composites is found to be negative, which confirms that the small polarons are responsible for thermoelectric transport.

In the low-temperature range below T_s, the Phonon and Magnon-drag effects (S_{ph} and S_{mag}) add to the diffusion (S_d) [22,23]. The Magnon-drag effect is produced because of the existence of electron–Magnon scattering, while the Phonon-drag is because of electron–Phonon scattering. The whole S –T range, shown in Fig. 3, was analyzed using the following relation [20] (note that $n_{ph} \alpha T^3$, $n_{mag} \alpha T^{3/2}$):

$$S = S_o + S_1 T + S_{3/2} T^{3/2} + S_3 T^3 + S_4 T^4 \tag{3}$$

where S_0 is a constant which accounts the low temperature variation of thermoelectric power and the parameters S_1, $S_{3/2}$, S_3, and S_4 are attributed to electronic diffusion process, electron–Magnon scattering or Magnon-drag (n_{mag}) effect, electron–Phonon scattering or Phonon-drag (n_{ph}), and spin fluctuations in FM phase, respectively.

There are other mechanisms behind the Phonon-electron drag contribution, such as Magnon-drag, impurities, and spin wave fluctuation. The Phonon drags effect on thermopower reductions is visible for lower temperature, wherein it disappears at 0 K. The magnitude of the considered parameters S_o, S_1, $S_{3/2}$, S_3 and S_4 are given in Table 3. Correspondingly, the Phonon-drag behavior is dependent on T^3 and the Magnon-drag behavior is dependent on $T^{3/2}$, as shown in Figs. 4 and 5.

We observed a strong contribution of electron–Magnon scatters $S_{3/2}$ >> S_3 >> S_4 at low temperature, and less possible contribution of Magnon-drag effect (S_3) as well as spin wave fluctuations (S_4) (Table 3). There is an overlap between the Phonon and Magnon-drag effects in a low-temperature region, thereby indicating that both of them might occur together at a low temperature. Thus, based on the aforementioned results, one can conclude that the Magnon and Phonon-drag effects contribute to the TEP of the samples.
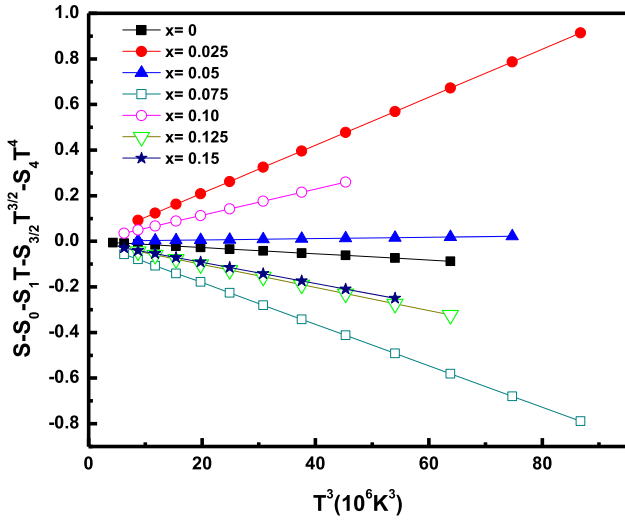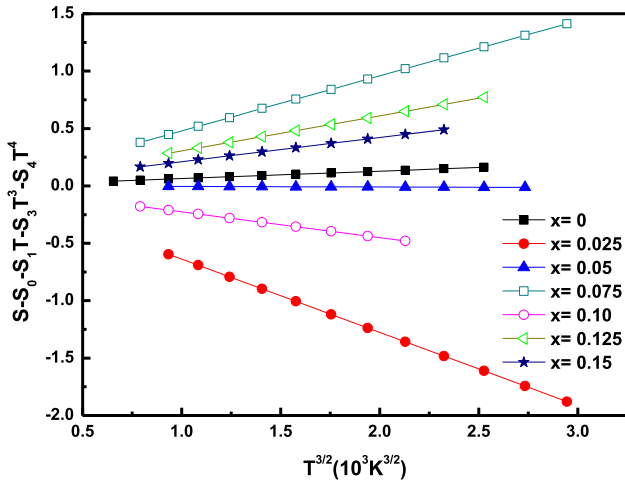
The power factor (S_2/ρ or $S_2\sigma$, where ρ is the resistivity determined from the ρ-T curves, which is recorded in a submitted paper) of the composites at RT is shown in Fig. 6. It can be seen that the power factor decreases with the increasing x content, and it reaches its highest value at x = 0.025 wt%. This is mainly because of the increasing AlO content, which serves as a barrier to blocking electron transport (the Seebeck coefficient), thereby causing an increase in the resistivity.

3.3. Magnetic properties

The magnetic susceptibility (χ), as a function of temperature, for LBMO/Al$_2$O$_3$ is shown in Fig. 7. All composites exhibit ferro- para-magnetic transitions at a certain temperature (T_C). The χ value decreases with the increasing Al content in the FM range. As discussed earlier, Al$_2$O$_3$ sits only at the grain boundaries and on the surfaces of the LBMO grain that causes an increase in non-magnetic or weak magnetic properties, which is responsible for the suppression of T_C and reduction of magnetization. Moreover, based on the double-exchange model, it is observed that there is a direct relationship between T_c and electronic bandwidth, which depends on the < Mn−O−Mn > bond angle and < Mn−O > distance, which is determined using the following approximate formula [24].

$$W \propto \frac{Cos\left[\frac{1}{2}(\pi - < Mn - O - Mn>)\right]}{d^{3.5}_{<Mn-O>}} \tag{4}$$

A small change in W has a significant effect on the magnetic properties of the composites. As presented in Table 4, the evolution of electronic bandwidth is in agreement with the T_C behavior. Besides, it is evident that the Ts values are below the T_C values, as presented in Table 4. Thus, it is observed in a FM semiconductor's range, wherein double exchange along with metallic behavior is expected to occur with ferromagnetism. In Fig. 7, it is observed that the susceptibility curve flattened significantly with a slow decline at temperatures lower than

Table 3
The best fit parameters obtained from thermoelectric power data of LBMO/Al$_2$O$_3$ (0 ≤ x ≤ 0.15) wt%.

Composite	S_0 (μV/K)	S_1 (μV/K^2)	$S_{3/2}$ (μV/K$^{5/2}$)	S_3 (μV/K^4)	S_4 (μV/K^5)
0	1.05E-02	−6.44E-04	6.43E-05	−1.37E-08	2.88E-11
0.025	−1.78E-01	7.32E-03	−6.38E-04	1.05E-07	−2.02E-10
0.05	4.52E-03	−6.40E-06	−4.71E-06	2.96E-09	−8.29E-12
0.075	1.17E-01	−5.22E-03	4.80E-04	−9.10E-08	1.87E-10
0.10	− 4.02E-02	2.26E-03	−2.26E-04	5.72E-08	−1.49E-10
0.125	1.07E-01	−3.56E-03	3.05E-04	−5.06E-08	9.58E-11
0.150	− 4.07E-02	−2.16E-03	2.11E-04	−4.62E-08	1.03E-10

Fig. 4. Phonon-drag behavior dependent on (T^3).

Fig. 5. Magnon-drag behavior dependent on ($T^{3/2}$).
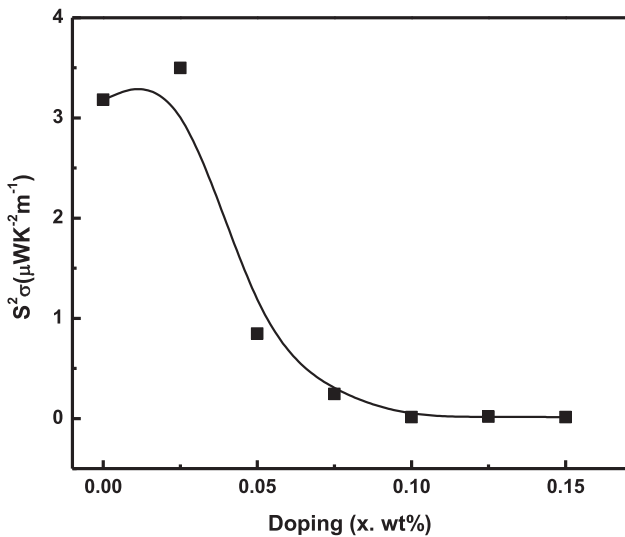
Fig. 6. Power factor versus doping content for $(La_{0.7}Ba_{0.3}MnO_3)_{1-x}/(Al_2O_3)_x$ composites, where $0 \leq x \leq 0.15$.

T_C in case of LBMO/Al$_2$O$_3$. The reason is as follows. In bulk samples the grain boundaries significantly contribute to the transport properties. The grain boundaries contain a large number of defects and magnetic spins. These spins respond to the exciting magnetic field when the temperature of the system is increased gradually. Thermal energy liberates the spins and allows them to align with the external field, thereby causing an increase in susceptibility with the increasing temperature (below T_C). However, with further increase in temperature, susceptibility starts reducing because of the increased thermal fluctuation of the spins, and ultimately the system undergoes the FM to paramagnetic phase transition at T_C. The paramagnetic susceptibility data can be usually approximated by using the Curie–Weis law, i.e., $\chi(T) = H/M = C/(T - \theta_C)$; where θ_C is the experimental T_C determined by the interception of the $1/\chi$ curve and C from linear fitting of the χ^{-1} data in the high-temperature region, as shown in Fig. 8. We calculated the effective paramagnetic moment (μ_{eff}) estimated from the Curie constant, which is defined as follows:

$$C = \frac{N_{Mn}\mu_{eff}^2\mu_B^2}{3K_B}$$
(5)

where N_{Mn} is the number of *Mn* ions per unit volume, μ_B is the Bohr magneton, and k_B is the Boltzmann constant.

$$N_{Mn} = N_{mol}\left(\frac{N_A}{molar\ volume}\right) \cdot x_{doping}$$
(6)

The theoretical values of the effective paramagnetic moments μ_{eff} are obtained from

$$\mu_{eff} = g\sqrt{\bar{S}(\bar{S}+1)}$$

where

g is the Landefactor ≈ 2, $\bar{S}_1 = 2(Mn^{3+})$ *and* $\bar{S}_2 = \frac{3}{2}Mn^{4+}$

So

$$\mu_{eff} = g\sqrt{xS_1(S_1+1) + (1-x)S_2(S_2+1)}$$
(7)

The θ_C, μ_{eff} (exper.), and μ_{eff} (thero.) values are presented in Table 4. It is observed that θ_C is positive (indicates FM interaction between spins); besides, it has approximately the same value and trend as those of T_c. The slight drop in the μ_{eff} value suggests a change of crystal field and Landé factor (g) with the increasing Al content.

4. Conclusion

In this study, we investigated the TEP and magnetic properties of $(La_{0.7}Ba_{0.3}MnO_3)_{1-x}/(Al_2O_3)_x$ composites. The crystal structure analysis presented that the composites still exhibit a single-phase rhombohedral ($R\bar{3}C$) structure despite adding the non-magnetic Al$_2$O$_3$ phase. There is no reaction between the LBMO matrix and Al$_2$O$_3$ content. The composite of x = 0.075 has the largest cell volume. All composites show both signs of S. The conduction mechanism is dominated by the mixed charge carriers of electrons and holes. The analysis of $S(T)$ in the low-temperature region demonstrated that both S_m and S_g contribute with S_d. Moreover, the values of E_s are lower than those of E_ρ, which confirmed SPH. All composites suffer ferro-paramagnetic phase transition at a certain temperature (T_C). The χ value decreases with the increasing Al content. The susceptibility curve flattened significantly with a slow decline at temperatures lower than T_C.
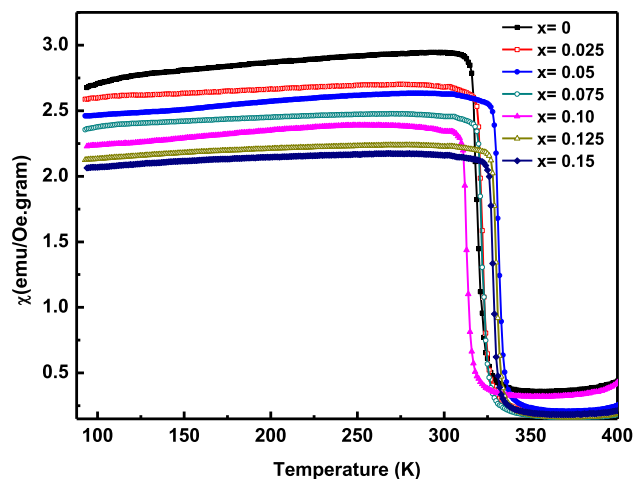
Fig. 7. Temperature dependence of susceptibility of LBMO/Al$_2$O$_3$, where $0 \le x \le 0.15$.

Table 4

T$_C$, θ$_C$, Ts(K) Transition temperature of TEP, the effective paramagnetic moments μ$_{eff.}$ (Exper., T > T$_C$) and μ$_{eff}$ (Thero., T > T$_C$) for (LBMO)$_{1-x}$/(Al$_2$O$_3$)$_x$ composites, where $0 \le x \le 0.15$ wt%.

Composite	T$_{C- \chi}$ (K)	θ$_C$ (K)	T$_s$ (K)	μ$_{eff}$ (Thero.)	μ$_{eff}$ (exper.)
0	316	315.3	195.5	4.31	2.38
0.025	319	319.61	215.5	4.85	1.85
0. 05	329	329.54	205.5	4.81	1.65
0.075	320	319.49	215.5	4.76	1.72
0.10	307	308.81	175.5	4.71	2.22
0.125	328	327.53	195.5	4.66	1.54
0.150	328	327.20	185.5	4.62	1.60

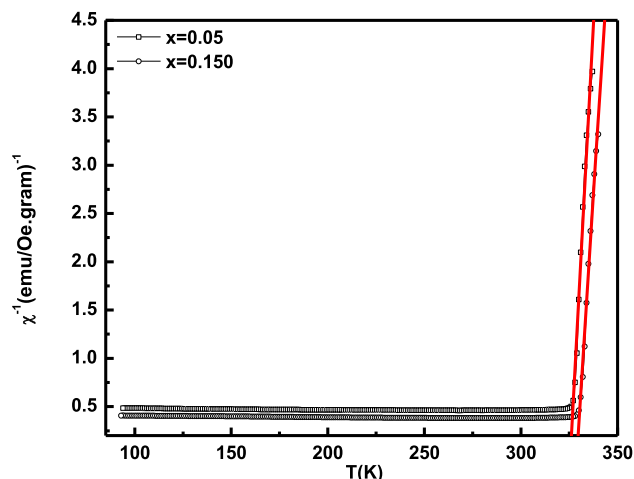**Fig. 8.** Inverse of magnetic susceptibility versus temperature of LBMO /Al$_2$O$_3$ composites, x = 0.05 and 0.15 wt%.

Compliance with ethical standards

Conflict of interest
The authors declare that they have no conflict of interest.

References

[1] D.M. Rowe, CRC Handbook of Thermoelectrics, Press, New York, 1995.
[2] T.M. Tritt, Science 283 (1999) 804.
[3] B.C. Sales, D. Mandrus, R.K. Williams, Science 272 (1996) 1325.
[4] D.-Y. Chung, T. Hogan, P. Brazis, M.R. Lane, C. Kamewurf, M. Bastea, C. Uher, M.G. Kanatzidis, Science 287 (2000) 1024.
[5] T. Caillat, J.-P. Fleurial, A. Borshchevsky, J. Phys. Chem. Solids 58 (1997) 1119.
[6] S. Sagar, V. Ganesan, P.A. Joy, Senoy Thomas, A. Liebig, M. Albrecht, M.R. Anantharaman, EPL (Europhys. Lett.) (2010).
[7] Atsuko Kosuga, YuriIsse, Yifeng Wang, Kunihito Koumoto, RyojiFunahashi, J. Appl. Phys. 105 (2009) 093717.
[8] Zhang Ya-Cui, Liu Jian, Li Yi, Chen Yu-Fei, Su Li Ji-Chao, Zhou Yu-Cheng Wen-Bin, Teng Wang Jin-ZeZhai, Wang Chun-Lei, Chin. Phys. B 26 (10) (2017) 107201.
[9] N. Panwar, D.K. Pandya, A. Rao, K.K. Wu, N. Kaurav, Y.-K. Kuo, S.K. Agarwal, Eur. Phys. J. B 65 (2008) 179.
[10] J. Rivas, L.E. Hueso, A. Fondado, F. Rivadulla, M.A. Lopez-Quintela, J. Magn. Magn. Mater. 221 (2000) 57.
[11] E. Rosenberg, G. Jung, M. Auslender, G. Gorodetsky, I. Felner, E. Sominski, A. Gedanken, Ya.M. Mukovskii, J. Appl. Phys. 99 (2006) 08Q305.
[12] L. Malavasi, M.C. Mozzati, S. Polizzi, C.B. Azzoni, G. Flor, Chem. Mater. 15 (2003) 5036.
[13] F. Chen, H.F. Liu, K.F. Wang, H. Yu, S. Dong, X.Y. Chen, X.P. Jiang, Z.F. Ren, J.-M. Liu, J. Phys.: Condens. Mater 17 (2005) L467.
[14] H.F. Mohamed, J. All. Comp. 712 (2017) 863.
[15] A.M. Ahmed, G. Papavassiliou, H.F. Mohamed, E.M.M. Ibrahim, J. Magn. Magn. Mater. 392 (2015) 27.
[16] A.M. Ahmed, Physica B 352 (2004) 330.
[17] A.M. Ahmed, A.K. Diab, H.F. Mohamed, J. Supercond. Nov. Magn. 24 (2011) 597.
[18] I.A. Abdel-Latif, Proceedings of the fifth Saudi physical society conference, AIP Conf. Proc. 1370 (2011) 108–115.
[19] C. Vazquez, M.C. Blanco, M.A. Lopez-Quintela, R.D. Sanchez, J. Rivas, S.B. Oseroff, J. Mater. Chem. 8 (4) (1998) 991.
[20] J. Yang, Y.P. Sun, W.H. Song, Y.P. Lee, J. Appl. Phys. 100 (2006) 123701.
[21] N.F. Mott, E.A. Davis, Electronic Process in Non Crystalline Materials, Clarendon, Oxford, 1979.
[22] S. Battacharya, S. Pal, A. Banerjee, H.D. Yang, B.K. Chaudhuri, J. Chem. Phys. 119 (2003) 3972.
[23] B.H. Kim, J.S. Kim, T.H. Park, D.S. Le, Y.W. Park, J. Appl. Phys. 103 (2008) 113717.
[24] A. Tozri, E. Dhahri, E.K. Hlil, Phys. Lett. A 375 (2011) 1528.